Iron distribution and speciation in a 3D-printed hybrid food using synchrotron X-ray fluorescence and X-ray absorption spectroscopies

Coline Schiell, Camille Rivard, Stéphane Portanguen, Valérie Scislowski,
Pierre-Sylvain Mirade, Thierry Astruc

Iron distribution and speciation in a 3D-printed hybrid food using synchrotron X-ray fluorescence and X-ray absorption spectroscopies

Coline Schiell [a,b], Camille Rivard [c,d], Stéphane Portanguen [b], Valérie Scislowski [a], Pierre-Sylvain Mirade [b], Thierry Astruc [b,*]

[a] *ADIV (Association pour le Développement de l'Institut de la Viande), 10 rue Jacqueline Auriol, 63039 Clermont-Ferrand, France*
[b] *Université Clermont Auvergne, INRAE, UR370 Qualité des Produits Animaux (QuaPA), 63122 Saint-Genès-Champanelle, France*
[c] *Synchrotron SOLEIL, L'Orme des Merisiers, Saint-Aubin, 91192 Gif-sur-Yvette, France*
[d] *INRAE, UAR1008 TRANSFORM, 44316 Nantes, France*

ARTICLE INFO

ABSTRACT

The bioavailability of iron from a food depends on its concentration and chemical form but also on dietary factors and nutrient interactions, which are affected by storage conditions and time. Here we investigated the time-course profile of iron in a hybrid 3D-printed food composed of alternating layers of liver and lentils after 0, 5, 7, 14 and 21 days of storage at 4 °C under oxygen or nitrogen packaging. Synchrotron X-ray fluorescence highlighted major variations in iron distribution in both the animal and plant parts of the food as a function of storage conditions. Fe—P and Fe—S positive spatial correlations pointed to iron-associated compounds. X-ray absorption near-edge structure spectroscopy showed spectral signatures specific to the animal and plant mixtures, and then highlighted interactions between animal and plant parts during food storage, with a change in iron forms in the plant part.

1. Introduction

Iron deficiency is the leading cause of anemia, which affects about 30 % of women aged 15–49 years, 37 % of pregnant women, and 40 % of young children (WHO, 2019). Iron is involved in an array of metabolic functions, and so iron deficiency can cause physical tiredness and weakness, respiratory and intestinal tract infections in adults, and impair psychomotor development in children (Shubham et al., 2020).

Dietary iron is found in two broad forms: heme iron (HI) and non-heme iron (NHI). HI is mostly found in animal-source food, although it does also make up part of plant hemoproteins such as cytochrome (Yruela, 2013). NHI is both found in animal-source and plant-source products.

In animal-source food, a large part of the iron is contained in Fe^{2+} form in the porphyrin ring of hemoglobin and myoglobin, which are responsible for oxygen storage and transport in blood and skeletal muscle, respectively (Collman et al., 1974). HI accounts for only 10 %–15 % of iron ingested, but it is highly bioavailable, with an intestinal absorption rate of around 15 %–40 % (Piskin et al., 2022). NHI is the main form of iron ingested, and it generally exists in two valence states: reduced ferrous (Fe^{2+}) and oxidized ferric (Fe^{3+}) forms. NHI can be found as free iron (ions) but also as complexed iron associated with proteins such as lactotransferrin and ferritin. As free iron and iron bound to low-molecular-weight compounds are more sensitive to molecule–iron interactions and dietary factors in general, NHI has a lower absorption rate (1 %–15 %) than HI (Shubham et al., 2020). However, in food Fe^{3+} complexes such as ferritin, the iron is protected against chelating agents by a protein shell, making it less reactive than in other iron forms (Zhao, 2010). For this reason, ferritin is now thought to hold potential as a new alternative source of dietary iron, and has thus attracted increasing research (Lv et al., 2015; Makowska et al., 2018; Zielińska-Dawidziak et al., 2023).

The transport of iron through the digestive tract and its subsequent absorption into intestinal cells involves several transporters and chain reactions. Fe^{2+} is more likely to be absorbed by enterocytes due to its better solubility compared to Fe^{3+} (Piskin et al., 2022), but the precise mechanisms governing iron uptake from ferritin remain unclear (Chang et al., 2023).

* Corresponding author.
  E-mail addresses: coline.schiell@adiv.fr (C. Schiell), camille.rivard@synchrotron-soleil.fr (C. Rivard), stephane.portanguen@inrae.fr (S. Portanguen), valerie.scislowski@adiv.fr (V. Scislowski), pierre-sylvain.mirade@inrae.fr (P.-S. Mirade), thierry.astruc@inrae.fr (T. Astruc).

Iron deficiency anemia is a major health concern, and there has been substantial research to address the factors that influence how the body absorbs iron. Ascorbic acid, folic acid, citric acid, cysteine-rich peptides, and even vitamin A can all be considered to enhance iron absorption, whereas phytates, tannins, polyphenols, and some minerals such as calcium, phosphorus and magnesium can inhibit iron absorption (Piskin et al., 2022). Furthermore, several studies have demonstrated that the addition of animal tissue to plant-based food not only improves NHI absorption but can also reduce the impact of certain inhibitors, in a process dubbed the 'meat factor' (O'Flaherty et al., 2019). The compound responsible for this increased uptake has not yet been clearly identified, but the literature states that partially digested products from animal tissue, such as cysteine-containing peptides, phospholipids, and mucopolysaccharides, could both reduce Fe^{3+} to Fe^{2+} and hold the iron in a soluble absorption-ready complex (Consalez et al., 2022).

A cost-effective way to remedy iron deficiency in many populations worldwide is to design new iron-rich hybrid foods engineered with nutritionally iron-rich ingredients to deliver an adequate supply of food iron. In this context, our team recently developed a 3D-printed model food containing iron from pork liver, chicken liver, and red lentils (*Lens culinaris L.*) in alternating layers (Schiell et al., 2023). Liver is particularly rich in iron, mainly in the form of ferritin and insoluble hemosiderin (67 % of total iron) with the remainder being HI in the form of hemoglobin (Archundia-Herrera et al., 2024; Shubham et al., 2020). The few studies that have been carried out in lentils have shown that about 69 % of the total lentil iron is present in the form of phytoferritin (Hoppler et al., 2009), while the rest of the iron corresponds to other iron complexes and soluble Fe^{2+} and Fe^{3+} (Quinteros et al., 2001). However, the chemical form and level of interaction of the iron with surrounding components is likely to affect its bioavailability, which warrants research into the fate of iron in food during processing and storage. In our previous study, the 3D-printed hybrid food showed a drop in HI content over the first 7 days of storage in an oxidizing atmosphere (Schiell et al., 2023). This result suggests a change in iron state during food storage. But given the novelty of 3D-printed hybrid food, the time–course change in oxidative status of iron and its diffusion and interaction in the liver/lentils interface matrix is still unknown.

Advances in synchrotron radiation now enable analysis of a multitude of biological samples. Over the past few years, X-ray fluorescence and absorption spectroscopy have been used to determine the elemental distribution and redox state of Fe in a number of earth materials (Henderson et al., 2014), but rarely in food applications. There has been a number of studies investigating iron in plant species, particularly cereals and pulses in the context of biofortification (De Brier et al., 2016; Grillet et al., 2014; Pongrac et al., 2016; Singh et al., 2013), but none to our knowledge have been carried out on lentil seeds. Likewise, only one study has used these techniques to investigate iron in animal-source material (Hasegawa et al., 2023).

Synchrotron X-ray has high spectral resolution and can acquire data under cryogenic conditions, making it well suited to *in situ* studies of the iron in food material. Micro-X-ray fluorescence (μ-XRF) imaging can map the spatial distribution of iron in food, and X-ray absorption near-edge structure spectroscopy (XANES) can capture the iron's oxidation state and atomic environment.

Using synchrotron X-ray techniques, the present study aims to investigate the time–course distribution of the forms of iron at the interface of lentil and liver layers in a 3D-printed hybrid food as a function of matrix type, time, and storage conditions, as these parameters are likely to affect iron bioavailability.

2. Materials and methods

2.1. Processing the iron-rich food

2.1.1. Preparation of raw materials for subsequent 3D food printing

To manufacture the iron-rich hybrid food, the animal part and plant part were prepared separately before being assembled together during the printing process, as described by Schiell et al. (2023). Briefly, the animal part is composed of raw chicken liver (Celvia, Saint-Jean-Brévelay, France) and raw pork liver (Tradival, Roanne, France) (ratio 70:30 w/w) previously ground then mixed with raspberry vinegar (2 % w/w) and salt (0.5 % w/w). This animal mixture was then pre-cooked in a water bath at 50 °C for 15 min to improve its printability. The plant part is composed of dry red lentils (Sabarot, Chaspuzac, France) cooked for 15 min in unsalted boiling water (ratio 1:5 w/w) and then blended to a puree. To improve technological, organoleptic and nutritional properties, lupin flour (10 % w/w), peanut oil (3 % w/w), curry powder (0.4 % w/w) and salt (0.4 % w/w) were added to the lentil puree. The animal and plant parts were stored overnight at 4 °C before printing.

2.1.2. Printing process

A model food was designed in the form of a cylindrical cookie (⌀ 70 × 16 mm; 5 layers) in alternating layers sandwiching the animal part inside plant-part layers in an animal/plant ratio of about 20:80. A series of these foods was manufactured using a 'Foodini' commercial extrusion-based 3D-printer (Natural Machines, Barcelona, Spain) with a 4 mm nozzle diameter, working at room temperature.

2.1.3. Post-printing process

After printing, the 3D-printed hybrid foods were baked at 180 °C with 70 % steam for 5 min (to a core temperature of 72 °C) using an electric oven (HMI Thirode, Emeraude III+, Mitry-Mory, France) to stabilize the food 3D geometry and guarantee food safety. After cooling down to room temperature, the 3D-printed products were packed in plastic trays (14.5 × 21.5 × 5 cm) under two different modified atmospheres (MAP), i.e. O_2-MAP with 70 % O_2 + 30 % CO_2 and N_2-MAP with 70 % N_2 + 30 % CO_2, using a sealing machine (Multivac, C500, Wolfertschwenden, Germany), then stored at 4 °C for up to 21 days.

2.2. Sample preparation

2.2.1. Sample preparation for iron assays and bulk X-ray analysis

The main raw materials used to prepare the food, i.e. the different types of liver and lentils, the final animal mixture (30 % pork liver + 70 % chicken liver) and plant mixture (lentils + lupin flour, peanut oil, curry powder, and salt) were separately powdered with liquid nitrogen (−196 °C) and stored at −80 °C. Furthermore, at each stage of time–course analysis, a 75 % sample of the food was powdered with liquid nitrogen (−196 °C) and stored at −80 °C.

For bulk X-ray analysis, 1 g of these frozen powered samples was packed into a well on a copper support covered with Ultralene® film. Reference samples of freeze-dried horse spleen ferritin (F4503; Sigma-Aldrich, St. Louis, MO) and porcine hemoglobin (H4131; Sigma-Aldrich, St. Louis, MO) were prepared by mixing 15 mg of ferritin with cellulose and with 150 mg of hemoglobin powder, and pressing the mixture into 6 mm pellets that were then placed in copper holders to optimize fluorescence mode conditions. Hemoglobin and ferritin were targeted here as they are the main forms of iron in our model food composed of liver and lentils. The bulks were prepared with hemoglobin predominantly in the non-oxidized form (Fe^{2+}). To avoid oxidation of the iron in hemoglobin (Fe^{2+} to Fe^{3+}) as much as possible, we were careful to open the sample vial at the very last moment and to manufacture the bulks extemporaneously as quickly as possible.

2.2.2. Sample preparation for in situ XRF mapping and XANES analysis

At each stage of time–course analysis, core samples (0.5 × 1 × 0.5 cm³) from the remaining 25 % food were cut at the animal/plant interface and cryofixed for 30 s in liquid nitrogen-cooled isopentane (−160 °C) on the same day to stop the reactions and preserve the structures. The samples were stored at −80 °C before analysis. Just before the acquisitions, 10 μm-thick cryosections were cut perpendicular to the printing layer at −20 °C using a Leica CM 1950 cryomicrotome

(Leica Biosystems, Nussloch, Germany). The cryosections were then sandwiched between two layers of Ultralene® film and clipped onto platelets (VeroClear material, Objet30 Pro, Stratasys Ltd., Eden Prairie, MN) that were screwed on copper holders before analysis by μ-XRF and XANES. The sections were kept in a liquid nitrogen bath during transfer between the laboratory and the beamline.

2.3. Measurements of HI and NHI contents

HI and NHI contents were assayed to track their time–course in the food according to storage conditions and time. HI content was determined from 5 g of ground sample by spectrophotometry at 640 nm as described by Hornsey (1956) and Schiell et al. (2023). NHI content was determined from 1 g of ground sample by spectrophotometry at 562 nm using ferrozine reagent following the procedure described by Ahn et al. (1993) and Schiell et al. (2023). Total iron was calculated by summing HI content and NHI content. Analyses were performed in triplicate.

2.4. Synchrotron XRF imaging and XANES analyses

2.4.1. Experimental set-up

Iron distribution and speciation were determined using XRF and XANES spectroscopies on the LUCIA beamline ('Line for Ultimate Characterization by Imaging and Absorption') (Vantelon et al., 2016) at the SOLEIL Synchrotron radiation facility (Gif-sur-Yvette, France). The X-ray beam was monochromatized using a double-crystal Si (311) monochromator for XANES bulk analyses and a double-crystal Si (111) monochromator for μ-XRF and μ-XANES analyses to obtain higher flux. Monochromator energy was calibrated by setting the maximum of the first derivative of a metallic Fe foil XANES spectrum at 7111.9 eV. Analyses were conducted with an unfocused beam (2×2 mm^2) or with a 3.1×2.6 μm^2 (H x V) focused beam using Kirkpatrick-Baez mirrors. The fluorescence signal was collected using a 60 mm^2 mono-element Si drift diode array (Bruker AXS, Madison, WI). The experimental chamber was under vacuum to reduce the absorption and scattering of X-rays through the air, and equipped with a cryostat filled with liquid nitrogen (-150 °C) to limit ion diffusion in the sample during analysis. Samples were only analyzed once due to limited beamline time.

2.4.2. Data acquisition

μ-XRF mapping was conducted at 7.25 keV in continuous acquisition mode (Flyscan). Fast and large iron maps at low spatial resolution (150 μm steps, 50 ms acquisitions, 6×6 mm^2) were first collected to identify the interface before then collecting high-spatial-resolution maps (3 μm steps, 200 ms acquisitions, 1000×400 μm^2) around the animal-layer/plant-layers interface.

Data was pre-processed using Jupyter notebooks (https://jupyter.org) written at SOLEIL: i) the fluorescence spectra collected from each pixel of the map were normalized by the incident flux and corrected from the XRF detector deadtime value, ii) each spectrum was then deconvoluted using the *Fast XRF linear fit* plugin bundled with PyMCA software (Solé et al., 2007) to obtain fluorescence maps of Fe as well as phosphorus (P) and sulfur (S). μ-XRF is a powerful approach enabling simultaneous location mapping of several elements in a single acquisition, in cryogenic conditions that minimize diffusion in the sample. The μ-XRF maps were then normalized by the *NetCount* (XRF spectrum intensity subtracted from the baseline obtained during XRF fitting) to compare the relative amount of each element between samples without the influence of thickness differences between sections.

On six selected points of interest (POIs) on the μ-XRF maps, μ-XANES data was acquired in animal and plant parts on both sides of the interface. The μ-XANES spectra were recorded in fluorescence mode over the 7.04 to 7.30 keV energy range at an energy step of 0.2 eV and an acquisition time of 5 s/point in the pre-edge region (7105.2–7121 eV). Bulk XANES analyses were also collected at the Fe K-edge using the unfocused beam for powdered samples of raw and reference materials.

Spectra were processed using Fastosh software (Landrot, 2018). E_0 edge energy was chosen as the maximum of the first derivative of the XANES spectrum. The background was subtracted from the spectra using linear regression in the pre-edge region and polynomial regression after the edge to obtain a horizontal signal.

2.4.3. Data treatment

Determination of Fe oxidation state. Fe K-edge XANES is sensitive to Fe redox states, especially the pre-edge feature, which is located about 15–20 eV before the white line of the spectrum. The speciation of Fe combines the oxidation state of the iron, mainly Fe^{2+} or Fe^{3+}, and its local coordination environment, which corresponds to the number of atoms, molecules or ions bonded to iron. In this study, the speciation of the Fe was determined from the normalized integrated intensity and from the centroid of the energy position of the pre-edge features, as described by Wilke et al. (2001). In a first step, to extract the pre-edge, the background was fitted using Fityk software version 1.3.1 (Wojdyr, 2010) with two pseudo-Voigt functions (Fig. S1). To extract the pre-edge in the same way for all the XANES spectra, the position of the functions was fixed at 7121.0 eV and 7129.1 eV. After extraction, the pre-edge peak was deconvoluted into two pseudo-Voigt functions fitting the spectral region from 7100 to 7122 eV using positions fixed at 7113.22 eV and 7114.27 eV, which correspond to the energy of the hemoglobin (Fe^{2+}) and ferritin (Fe^{3+}) references, respectively (Fig. S2). The shape of the pseudo-Voigt functions was set at 0.5, and the same width was applied for both functions, as in Wilke et al. (2001). Pre-edge characteristics such as position and area were then collected to calculate the position of the pre-edge centroid and the integrated intensity.

Processing of the distribution maps. The contrast of the elemental μ-XRF maps was adjusted to the same color scale with Fiji software (Schindelin et al., 2012) to cross-compare the maps. μ-XRF intensity profiles were computed on a selected band of 30 pixels, i.e. 90 μm wide, to exclude areas giving a null signal due to absence of material. Based on these profiles, average intensity values for Fe, P and S were calculated in the animal and plant areas for each experimental condition.

Furthermore, regions of interest (ROIs) were selected in the animal and plant areas to study the specific distribution of Fe as well as P and S in these zones according to experimental conditions, by extracting the intensity of each pixel in the ROI and plotting the correlation diagram between iron and these elements. For each μ-XRF map, three amyloplasts at different distances from the interface and two liver zones of the same size were selected, and we then calculated the averages for each area (plant and animal), after first checking that the distance to the interface did not influence the intensity of the elements studied (Fig. S3).

2.5. Statistical analysis

Statistical analyses were performed using Statistica software (Statistica, version 13.5; TIBCO Software Inc., Palo Alto, CA). Results are expressed as mean ± standard error of the mean (SEM). Variance analysis and comparisons of means were performed using a Fisher test followed by a post-hoc Tukey HSD test. Differences were considered significant at $p < 0.05$. Linear regression models were calculated from the scatterplots using Microsoft Excel 2016 software running under Windows 11.

3. Results

3.1. Iron content in raw materials and in subsequent 3D-printed foods

Table 1 and Table 2 report the forms of iron by content in raw materials and 3D-printed foods.

Total iron content was approximately four times higher in the animal-source preparations than in the plant-source preparations (Table 1). NHI was predominant regardless of the matrix, as its proportion was close to 80 % for the animal mixtures and 100 % for the

Table 1

Mean contents of HI, NHI and total iron measured on the raw materials and on final mixtures.

Samples	HI (mg/100 g)	NHI (mg/100 g)	Total Iron (mg/100 g)
Chicken liver (raw)	3.53 ± 0.07	13.77 ± 0.10	17.30 ± 0.04
Pork liver (raw)	3.99 ± 0.04	16.02 ± 0.09	20.01 ± 0.13
Animal mixture (raw)	4.09 ± 0.12	15.98 ± 0.23	20.07 ± 0.18
Animal mixture (pre-cooked)	3.80 ± 0.02	17.78 ± 0.17	21.58 ± 0.17
Red lentils (cooked and mixed)	n.d.	4.18 ± 0.04	4.18 ± 0.04
Plant mixture	n.d.	5.61 ± 0.40	5.61 ± 0.40

Data are expressed as means $\pm$ SEM ($n = 3$) of the edible portion. Total iron = HI + NHI. n.d.: not detected.

Table 2

Effect of time in storage and MAP on the forms of iron measured in the 3D-printed food.

Days in Storage	HI (mg/100 g)		NHI (mg/100 g)		Total Iron (mg/100 g)	
	N_2-MAP	O_2-MAP	N_2-MAP	O_2-MAP	N_2-MAP	O_2-MAP
0	0.89 [g] ± 0.01	0.89 [g] ± 0.01	9.25 [ab] ± 0.05	9.25 [ab] ± 0.05	10.14 [abc] ± 0.05	10.14 [abc] ± 0.05
5	0.81 [f] ± 0.01	0.36 [c] ± 0.01	10.22 [b] ± 0.38	8.78 [a] ± 0.06	11.03 [c] ± 0.37	9.14 [ab] ± 0.05
7	0.79 [f] ± 0.02	0.33 [bc] ± 0.01	8.44 [a] ± 0.32	8.88 [a] ± 0.04	9.23 [ab] ± 0.31	9.20 [ab] ± 0.04
14	0.69 [e] ± 0.00	0.28 [ab] ± 0.00	8.98 [ab] ± 0.31	8.67 [a] ± 0.30	9.67 [ab] ± 0.31	8.95 [a] ± 0.30
21	0.62 [d] ± 0.01	0.26 [a] ± 0.01	8.76 [a] ± 0.22	8.95 [a] ± 0.30	9.38 [ab] ± 0.21	9.21 [ab] ± 0.29

Data are expressed as means $\pm$ SEM ($n = 3$). In each column, lowercase superscript letters (a to g) indicate significant differences between samples for different forms of iron (HI, NHI, total iron) according to MAP (O_2-MAP and N_2-MAP) ($p < 0.05$). O_2-MAP corresponds to 70 % oxygen (O_2) + 30 % carbon dioxide (CO_2). N_2-MAP corresponds to 70 % nitrogen (N_2) + 30 % carbon dioxide (CO_2).

plant mixtures. As expected, only the animal mixtures contained a significant HI content. Total iron concentration of the animal-source mixture increased slightly after pre-cooking, likely due to water losses, leading to an increase in iron concentration in the matrix. Similarly, the addition of lupin flour to the lentils increased the iron content of the plant mixture (Mazumder et al., 2021).

Iron assays carried out on hybrid foods (Table 2) demonstrated that HI decreased with storage time regardless of storage conditions, although the decrease was faster and greater under O_2-MAP. Although this decrease was significant (0.89 to 0.26 mg/100 g), it had no effect on total iron content of the food due to the much higher NHI content. Overall, there was no significant impact of time or MAP method on the total iron content of the food (except for the sample at D5/N_2-MAP, where total iron content was slightly higher).

3.2. Iron distribution in the hybrid food

Besides the quantification of iron at whole-food level, µ-XRF imaging was conducted at the animal/plant interface over a 1 mm-wide zone to characterize the iron distribution close to this interface. µ-XRF maps of spatial Fe distribution and associated Fe, P and S profiles are presented in Figs. 1 & 2, respectively.

The iron µ-XRF maps (Fig. 1) and iron distribution profiles (Fig. 2) demonstrated that average iron signal was significantly higher in samples stored under O_2-MAP vs N_2-MAP (575 $\pm$ 6 counts vs 311 $\pm$ 4 counts; $p < 0.05$). A slight but significant decrease ($p < 0.05$) in the iron signal was detected from day 5 in storage, i.e. 434 $\pm$ 5 counts at day 5 vs 395 $\pm$ 6 counts at day 14. The high-intensity regions on day 21 under O_2-MAP

are probably due to a cutting artefact.

In agreement with the iron assays presented in section 3.1., on average, the animal part (on the right) was significantly ($p < 0.05$) richer in iron (590 $\pm$ 5 counts) than the plant part (on the left) (290 counts $\pm$5 counts), despite the hotspots.

Iron was heterogeneously distributed in the plant part, with sizeable local variations in the peaks on the profiles, especially for samples stored under O_2-MAP (Fig. 2), which increased the mean value of the Fe signal for this MAP condition (201 $\pm$ 4 counts under O_2-MAP vs 407 $\pm$ 7 counts under N_2-MAP). Iron distribution did not change significantly according to time in storage. Iron hotspots were observed in amyloplasts (Fig. 1) in between starch grains identified by histological staining (Fig. 1b).

In the animal part, the maps and profiles indicated a relatively homogeneous iron distribution, although the Fe signal measured was higher on average under O_2-MAP than N_2-MAP (at 717 $\pm$ 7 counts vs 448 $\pm$ 3 counts under N_2-MAP; $p < 0.05$).

3.3. Atomic environment of iron

The distribution profiles of P and S, which are elements known to complex iron (Estévez et al., 2020; Singh et al., 2013), were acquired to investigate their colocalization with iron at the animal/plant interface (Fig. 2). Signal intensities for P and S were significantly higher on average in the animal part (434 $\pm$ 2 counts and 645 $\pm$ 2 counts, respectively) than in the plant part (127 $\pm$ 2 counts and 188 $\pm$ 2 counts, respectively; $p < 0.05$). These values remained globally constant regardless of storage time and packaging conditions. Overall, the P and S profiles overlapped the iron profile. Fe and P colocalization was evidenced by the Fe—P correlation plots and merged µ-XRF maps (Fig. 3a and c). Fe and S colocalization analysis gave similar results to the Fe—P colocalization analysis (Fig. S4).

The distribution of the dots demonstrated a positive relationship between Fe and P for all the ROIs selected. Nevertheless, these plots also indicated differences in correlations between the elements in the liver and lentil matrices, reflecting their different iron speciation. According to previous observations, the pattern of dots for lentil was less dense and more heterogeneous compared to the pattern of dots for liver (Fig. 3a), resulting in a significantly ($p < 0.05$) higher coefficient of determination for the animal part ($r^2 = 0.96$) than the plant part ($r^2 = 0.85$). Overall, the slope variation of the scatterplot in Fig. 3b highlighted a change in Fe—P interactions in the sample over the course of day 0 to day 21 in storage. The slope for the lentil and liver parts under N_2-MAP increased significantly with time in storage. The difference between N_2-MAP and O_2-MAP was also illustrated by Fig. 3c, which gives an example of Fe and P distribution during storage. In the plant part, Fe and P appeared to be more positively colocalized in the amyloplasts under O_2-MAP whereas their distribution appeared to be less positively colocalized under N_2-MAP, with P localized in amyloplasts and Fe localized around them. Fe—S correlation plots also followed this pattern (Fig. S4).

3.4. Iron speciation

Fe K-edge XANES spectra were used to study Fe oxidation state and Fe local coordination geometry by deconvolution of the pre-edge and by extracting the centroid and integrated pre-edge intensity values. Fig. 4 presents the Fe K-edge normalized XANES spectra, especially for pre-edges of raw materials and references. Fig. 5 and Table S1 chart the pre-edge features of all samples.

For the references, the centroid of the normalized Fe XANES were determined at 7113.22 eV for hemoglobin (Fe^{2+}) and 7114.27 eV for ferritin (Fe^{3+}), with a shift of about 1.05 eV between the two forms (Fig. 4b). As shown in Fig. 4b, c and Fig. 5, the energy position of the centroid for plant-based mixtures (7114.07 eV for boiled red lentils (RL) and 7114.21 eV for plant mixture (PM)) was closer to ferritin (Fe^{3+}) than hemoglobin (Fe^{2+}). The energy position of the animal-based mixtures (AM1 and AM2) (7113.82 eV on average) was intermediate between
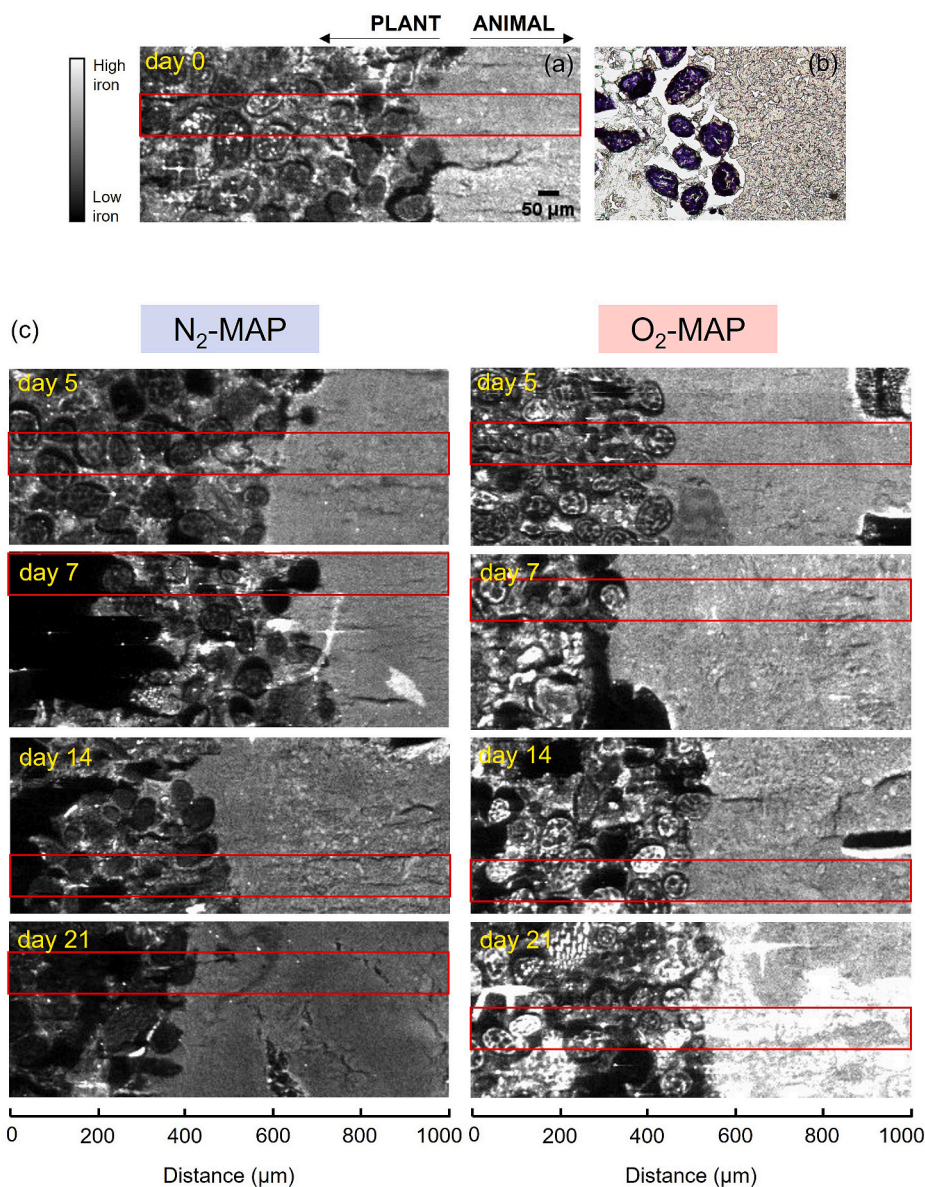
Fig. 1. µ-XRF maps of iron in cryosectioned foods at days 0 (1-a), 5, 7, 14 and 21 of storage under N_2-MAP compared to samples stored for the same period under O_2-MAP (1-c). The red rectangle corresponds to the area where the profiles were calculated, with the plant part on the left-hand side and the animal part on the right-hand side. The applied grayscale is similar for all the maps. Locations of amyloplasts with starch grains (in dark blue) were confirmed by histological staining with Lugol (1-b).

hemoglobin (Fe^{2+}) and ferritin (Fe^{3+}). Pork liver (PL) appeared to be more oxidized, as it shifted more towards higher energies (7114.09 eV) than the chicken liver (CL) (7113.61 eV) and the other animal mixtures (7113.77 eV for AM1 and 7113.80 eV for AM2). Raw and final precooked animal mixtures were closer to the spectrum of chicken liver (CL), which is consistent with the proportions used (70 % CL and 30 % PL). The main difference between patterns of animal and plant mixtures was their integrated pre-edge intensities (0.15 on average for animal-based mixtures *vs* 0.48 for plant-based mixtures; $p < 0.05$).

For the final foods, µ-XANES spectra at six POIs per µ-XRF map were spread across the width of the section. The pre-edge centroid position and integrated intensity of each POI were then positioned on the scatterplot with pre-edge features of bulk XANES in Fig. 5.

No clear trend emerged in terms of the impact of storage conditions, although the POIs under N_2-MAP appeared to be more dispersed due to a greater diversity of iron forms. A comparison of the results at different storage times after day 0 also found no significant differences (**Fig. S5**

and Table S2), which is why the storage times were not specified on the plots in Fig. 5. At day 0, the POIs spectra selected in the animal area (POI1 and POI2) were close to those of the animal mixtures (AM1 and AM2) and showed a more reduced form of iron (Fig. 5a and b). Similarly, the POIs spectra selected in the plant area (POI4 to POI6) were close to the more oxidized form of plant mixtures (RL and PM). POI3 is an intermediate point between the animal and plant parts.

Across the entire period of storage from day 5 to day 21 (Fig. 5c), the plots of animal POIs clustered around the spectra for animal-based mixtures under both N_2-MAP and O_2-MAP. The plots of plant POIs were more scattered, reflecting a heterogeneity of the iron forms in the plant mixture within the same sample. Surprisingly, many of the spectra acquired in the plant part displayed patterns typical of the animal-mixtures spectra, with a more reduced form of iron, and from the earliest times in storage.
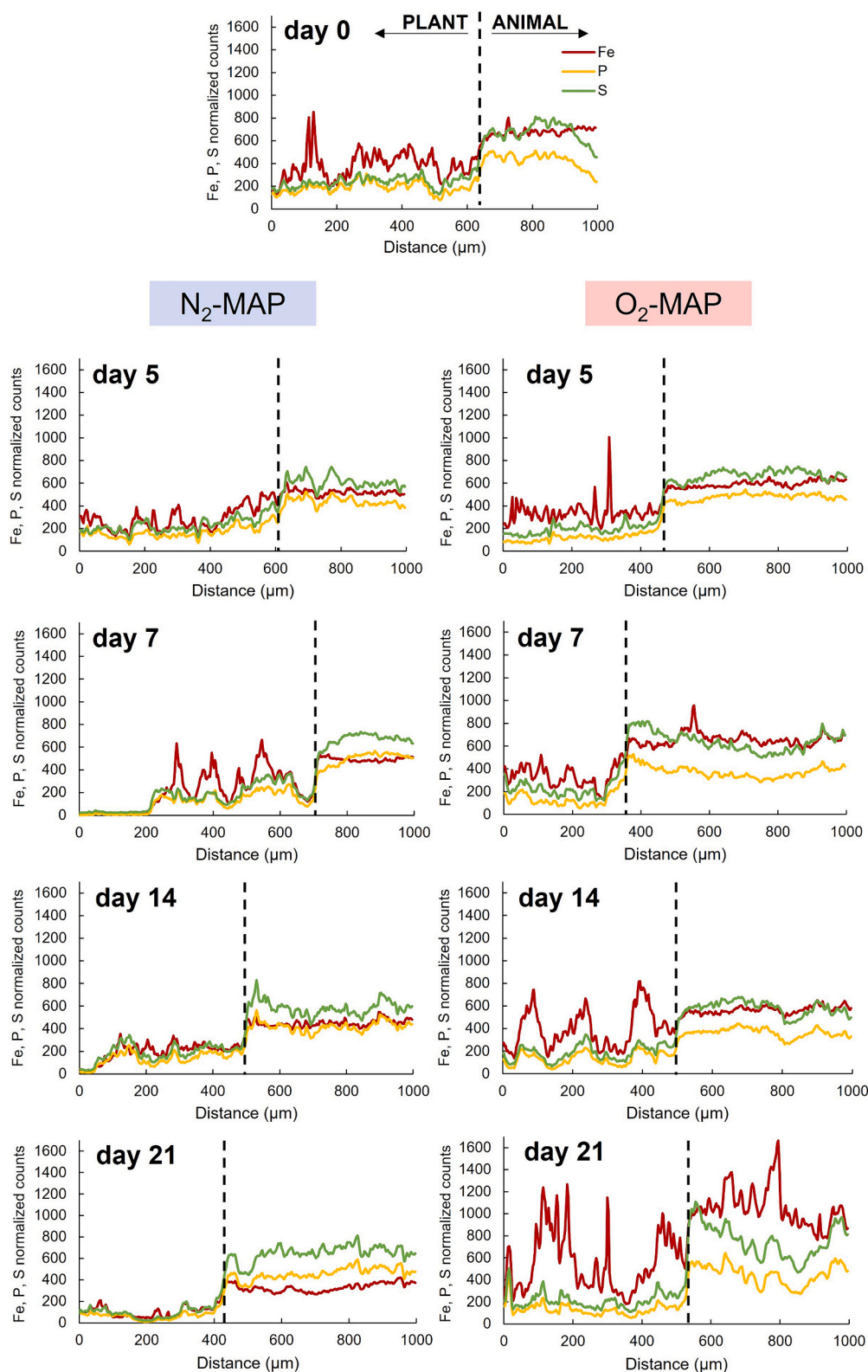
Fig. 2. Profiles of iron (Fe), phosphorus (P) and sulfur (S) extracted from μ-XRF maps in food samples at days 0, 5, 7, 14 and 21 of storage under N$_2$-MAP compared to samples stored for the same period under O$_2$-MAP. The dashed black line marks the plant/animal interface, with the plant part on the left-hand side and the animal part on the right-hand side.

4. Discussion

From a nutritional point of view, the uptake and assimilation of dietary iron depends both on the quantity of iron ingested and its form.

The total iron content found here for raw pork liver (20.01 ± 0.13 mg/100 g) was consistent with Tomovic et al. (2015) (19.5–23.9 mg/100 g) and Mullen and Álvarez (2016) (23.3 mg/100 g). The total iron content of the chicken liver (17.30 ± 0.04 mg/100 g) was between the
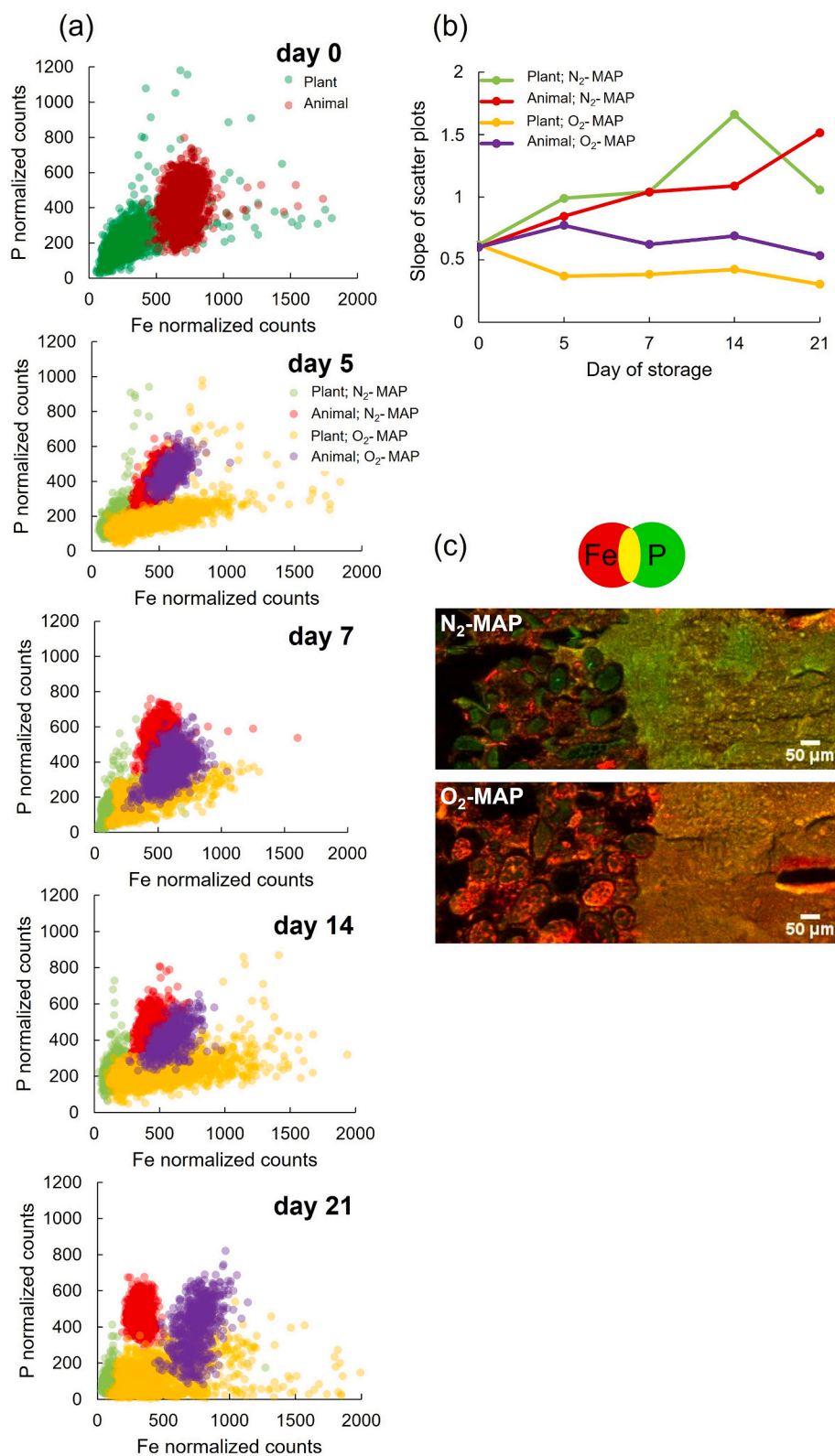
Fig. 3. (3-a) Fe—P correlation plots extracted from μ-XRF maps from day 0 to 21 according to storage conditions (O$_2$-MAP or N$_2$-MAP) and areas (animal or plant). (3-b) Time–course of the slope of the scatterplots for animal and plant parts during storage. (3-c) Comparison of merged μ-XRF maps of Fe and P for samples stored under O$_2$-MAP and N$_2$-MAP for 14 days. The color scales are the same for both maps.

8.99 mg/100 g found by Mullen and Álvarez (2016) and the 25.8 mg/ 100 g found previously in Schiell et al. (2023). This variability in chicken liver iron content may be due to differences in feed composition, genetics, breeding, or even geographical variations (Leonhardt & Wenk,

1997). The total iron content found here for cooked and mixed red lentils (4.18 ± 0.04 mg/100 g) was between the range of values observed by Quinteros et al. (2001) (2.01–2.25 mg/100 g) and Podder et al. (2021) (5.9–7.6 mg/100 g). These differences between studies are
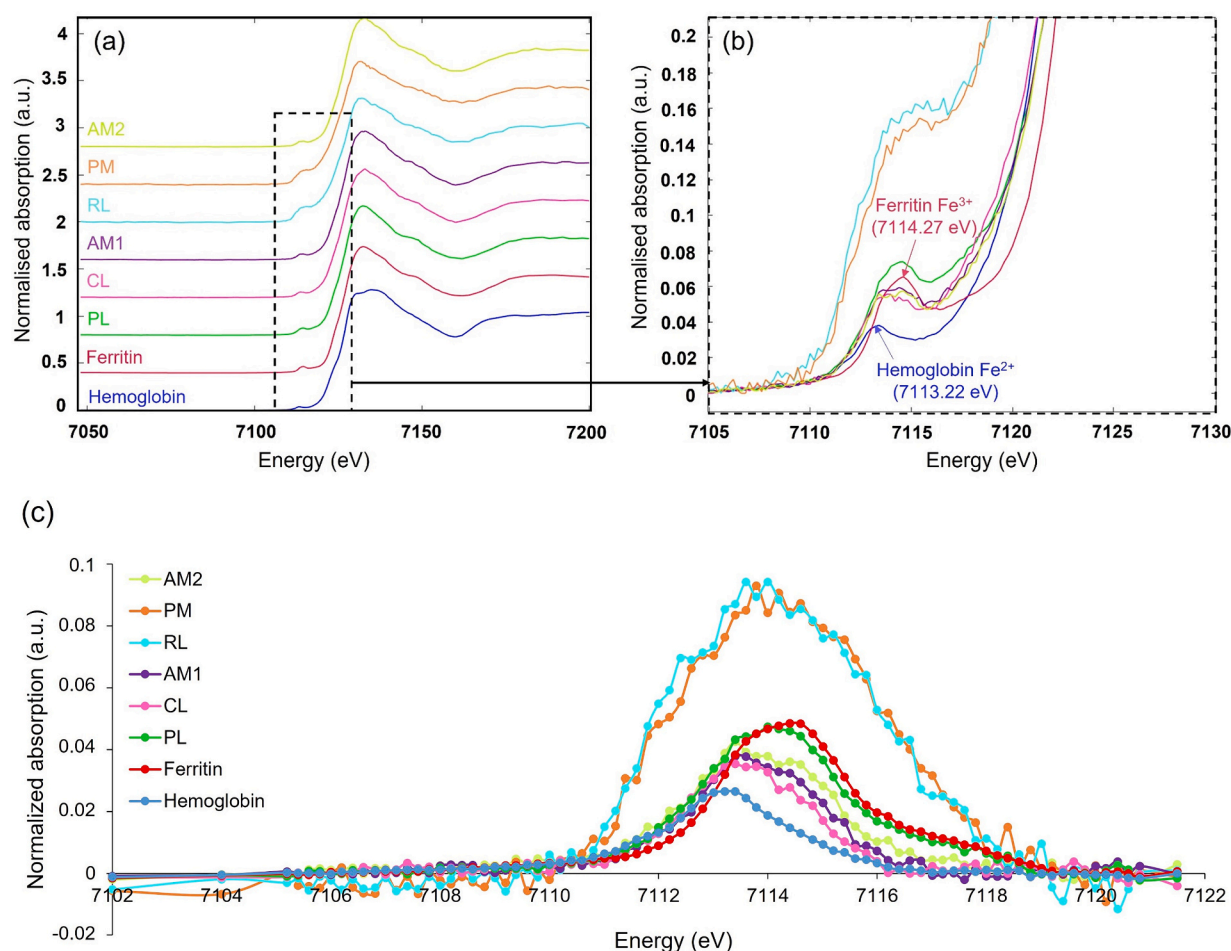
Fig. 4. (4–a) Fe K-edge normalized XANES spectra of raw materials and references. (4-b) Closer analysis of the pre-edge region. (4-c) Extracted pre-edge after subtraction of the background. CL: raw chicken liver; PL: raw pork liver; AM1: raw animal mixture; AM2: pre-cooked animal mixture; RL: boiled red lentils; PM: plant mixture. Hemoglobin and ferritin are the references.

probably due to variations in lentil cultivar, soaking process and cooking methods, all of which can affect iron content. The final plant mixture was richer in iron than lentils alone as the lupin flour used in the recipe also provided some iron (Mazumder et al., 2021).

The combination of the animal mixture and the plant mixture in alternating layers resulted in an average food iron content of around 10 mg/100 g, mostly composed of NHI. This result is lower than in our previous study that found an iron content close to 16 mg/100 g, due to the compositional variability of the raw materials used. Nevertheless, this iron content would cover 100 % and 53 % of the Recommended Dietary Allowance (RDA) for young children and women aged 19–50 years respectively, so our hybrid food is suitable for anemic people (Institute of Medicine, 2001).

The variability in iron concentration observed by μ-XRF over the course of storage is unexpected insofar as the content of these non-volatile elements is theoretically constant, as was seen for total iron content determined by spectrophotometry (Table 1). Moreover, we did not observe any exudation from foods during storage, and the XRF signal was normalized to the incident flux and normalized by the *NetCount* to overcome any variations in sample thickness. Whatever the packaging conditions, the XRF maps and profiles nevertheless demonstrated that iron concentration at the animal/plant interface was higher for foods stored under O_2-MAP than foods stored under N_2-MAP. These results may indicate a change in iron distribution in the food according to storage conditions that was not observed for other elements such as P and S. Our previous study highlighted the impact of the storage conditions on food structure and iron oxidation state (Schiell et al., 2023) that

could drive iron migration at the animal/plant interface. A hypothesis would be that water transfers between the layers, influenced by storage conditions, lead to a change in iron distribution in the food. To a lesser extent, this heterogeneity in distribution may be also due to the heterogeneous composition of biological tissues, which naturally have compartments that are more or less rich in iron. Indeed, the distribution of iron within the samples was very different according to type of matrix, in relation to differences in their structure and specific chemical composition. The localization of iron in the plant area is consistent with the fact that iron in lentils is mostly stored in the form of ferritin (Hoppler et al., 2009), which is mainly found in the amyloplasts around the starch grains in plant cells (Briat et al., 2010). Ferritin is known to capture and induce the mineralization of iron in its cavity in the presence of oxygen, which also explains the higher concentration of iron in amyloplasts under O_2-MAP compared to N_2-MAP (Zhao, 2010). Chopping and grinding the liver to prepare the food may have caused these structures to break down and thus disperse the hemoglobin, ferritin and hemosiderin iron into the matrix, which would explain the more homogeneous distribution of iron in liver.

The bioavailability and absorption of iron is a complex mechanism to unravel as it is also influenced by the presence of enhancer and inhibitor compounds in foods (Piskin et al., 2022; Shubham et al., 2020). To address this issue, the atomic environment of the iron was studied to identify potential compounds that could bind iron and influence its bioavailability. In the lentils area, we targeted the colocalization between Fe, P and S as they are among the main components of iron-binding compounds used by plants as a chelation strategy (Singh
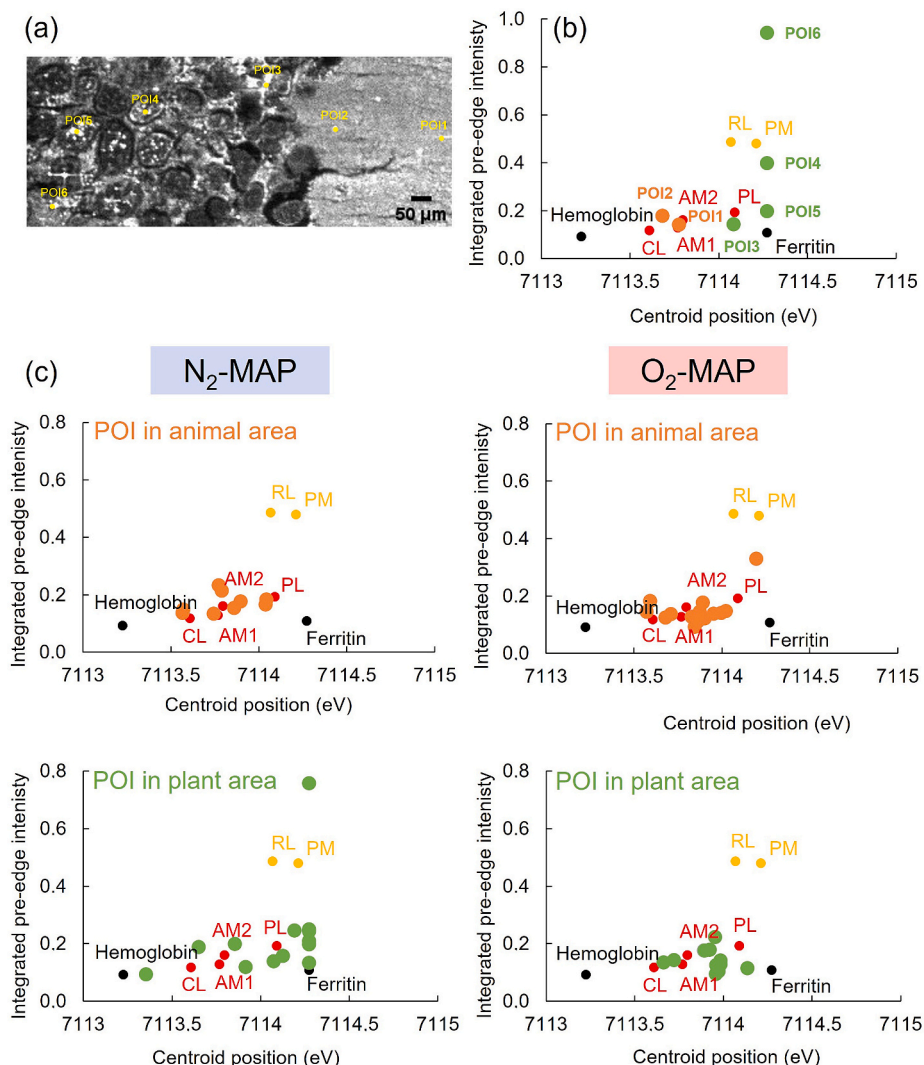
Fig. 5. (5-a) μ-XRF map of cryosectioned foods with the location of μ-XANES POIs (in yellow) at day 0. (5-b) Distribution of POIs at day 0 according to pre-edge features. (5-c) Distribution of all POIs combined (day 5 to day 21) according to pre-edge features for foods stored under N_2-MAP and O_2-MAP. Orange dots: POIs selected in the animal-part area; Green dots: POIs selected in the plant-part area; CL: raw chicken liver; PL: raw pork liver; AM1: raw animal mixture; AM2: pre-cooked animal mixture; RL: boiled red lentils; PM: plant mixture. Hemoglobin and ferritin are the references.

et al., 2013). Indeed, about 80 % of the total seed P is stored in the form of phytic acid (Bohn, Meyer, & Rasmussen, 2008). Here we found that the presence of P correlated with Fe in amyloplasts, which may promote the binding of iron to ferritin. Indeed, previous studies have demonstrated that the oxidation reaction-driven incorporation of iron into the ferritin envelope occurred in plastids with a high phosphate concentration (Li et al., 2009; Zhao, 2010). In liver, P is mainly found in phospholipids and metabolic enzymes (Cherian et al., 2023). The stronger Fe—P spatial correlation observed during food storage under N_2-MAP than O_2-MAP reflects an evolution in the atomic environment of iron, which could be due to new bonds between iron and P-containing compounds. However, another more plausible hypothesis, as demonstrated by our profiles, is a migration-induced decrease in the quantity of iron in this region with no equivalent change in P concentration under N_2-MAP, which would locally increase the Fe/P ratio. In contrast, under O_2-MAP, the scatterplots remained unchanged and the Fe—P correlations varied little or not at all, which makes it impossible to clearly identify changes in the atomic environment of iron under these conditions. Despite the presence of inhibitors of iron absorption such as phytates, the protein envelope of ferritin — found in both the animal and the plant parts — protects iron from the chelators mentioned above, and so iron bioavailability is less affected (Li et al., 2009). For this reason,

ferritin is thought to hold potential as new alternative source of dietary iron, and is attracting much research (Lv et al., 2015; Makowska et al., 2018; Zielińska-Dawidziak et al., 2023).

Compared to lentil seeds, where S is mainly found as biological sulfate (Singh et al., 2013), the higher content of S in the liver probably comes from S-containing amino acids, such as methionine or cysteine, included in proteins and/or involved in liver detoxification mechanisms (Estévez et al., 2020). The strong correlation of S with iron in both parts of the food, i.e. lentil and liver, promotes iron assimilation (Piskin et al., 2022). Like for P, the Fe—S correlations varied little during storage under O_2-MAP. The nutritional complementarity of lentils and liver in terms of iron content and chemical form is therefore an argument in favor of developing pro-health hybrid foods that are also in tune with current consumer trends.

The use of XANES as a complement to XRF provided an opportunity to take these hypotheses further by studying the iron speciation in the samples. Iron speciation analysis determines the proportions of bivalent and trivalent forms of Fe in the samples as a way to assess the bioavailability of the food iron as a function of its oxidation state, which depends on storage conditions. For spectral processing, hemoglobin and ferritin were the references for Fe^{2+} and Fe^{3+}, respectively. Results obtained for pre-edge peak energy, i.e. 7113.22 eV for hemoglobin

(Fe^{2+}) and 7114.27 eV for ferritin (Fe^{3+}) with a shift of about 1.05 eV, were consistent with the fact that the position of the pre-edge shifts towards a higher energy as oxidation state increases (Wilke et al., 2001). Nevertheless, the shift found here between the Fe^{2+} and Fe^{3+} forms was slightly lower than the shift measured by Hasegawa et al. (2023) (1.9 eV) and Wilke et al. (2001) (1.4 eV). This may be due to the diversity of hemoglobin oxidation states (Hasegawa et al., 2023; Wilson et al., 2013) and/or to the specific acquisition parameters and equipment used in each experiment. The acquisition of XANES spectra on raw materials highlighted typical spectral signatures for animal and plant mixtures, which are not often compared in the literature within the same series of analyses. First, we found a difference in the centroid of pre-edge energy between the animal-source and plant-source materials, showing the predominance of ferric iron in the plant mixture whereas the animal mixture contained both ferrous and ferric iron. We also found a difference in integrated pre-edge intensity between animal and plant tissue, which is mostly influenced by the Fe coordination geometry (Wilke et al., 2001). This can be explained by the diversity of compounds and bonds in which iron is involved in plants and animals.

As ferritin is an iron storage protein found in both animal and plant tissues, a spectral resemblance between these two types of ferritin might be expected. However, studies have demonstrated that ferritin iron absorption efficiencies differ according to ferritin source and even within ferritins from the same kingdom (Li et al., 2009; Srivastava et al., 2023). Indeed, despite their similar overall structures, ferritins from different sources are clearly distinguishable by their iron binding, oxidation, detoxification and mineralization properties (Chang et al., 2023). This may explain the difference in spectra between the reference horse spleen ferritin and our samples.

In addition, iron can also associate with other complexes in animal and plant parts, which may have impacted the average spectrum obtained. Indeed, the spectra from the animal-source raw materials showed an intermediate spectrum between hemoglobin Fe^{2+} and ferritin Fe^{3+}, supposing a combination of the two, and the Fe—P and Fe—S correlations highlighted other potential complexes. For the plant part, the Fe—P correlation could suggest complexation of iron by phytate (De Brier et al., 2016). Further analyses using plant references are needed to more precisely identify the forms of iron involved.

To carry out a more targeted analysis in relation to the iron distribution in our samples, μ-XANES spectra were acquired at POIs on the XRF maps. Some pre-edge patterns characteristic of animal-based mixture spectra were observed in the plant part of the samples under both N_2-MAP and O_2-MAP and at all timepoints after day 0 (Fig. 5). These observations may suggest a process of iron transfer from the animal part to the plant part, which would validate the hypothesis of a phenomenon of iron diffusion in between the layers of the hybrid food. This result raises questions about how iron bioavailability may be affected by movements through the matrix that lead to interactions with molecules to which iron is not naturally exposed. Another possible hypothesis is that the composition and therefore the physicochemical properties of the animal matrix may drive plant-origin iron ions to change speciation close to the animal/plant interface. In other words, it is possible that over the course of manufacturing and storage, some plant-origin iron ions may have changed speciation when they came into contact with the liver-based mixture. This change in iron speciation may be explained by the presence in liver of cysteine-containing peptides, and therefore sulfur amino acids (Seong et al., 2015), that can reduce Fe^{3+} to Fe^{2+} (Consalez et al., 2022), especially as the results demonstrated a spatial correlation between Fe and S. Similarly, the presence of ascorbic acid in the raspberry vinegar (Yildiz, 2023) present in the animal mixture may change the speciation of plant-source iron, as ascorbic acid has been shown to reduce Fe^{3+} to Fe^{2+} in some pulses (Grillet et al., 2014; Singh & Prasad, 2018).

Unfortunately, the limited synchrotron beamtime available to use meant that we were only able to run acquisitions on a few POIs in defined areas, and so we cannot reliably generalize our findings to the whole sample. Nevertheless, these results open up new avenues for reflection, although further experiments are needed before we can firmly conclude and validate these hypotheses.

5. Conclusion

This work investigated iron distribution and speciation in an iron-rich 3D-printed hybrid food composed of alternating layers of liver and lentils.

Results demonstrated that both storage conditions and time in storage had a significant impact on iron form and distribution in our multilayer model food. Iron signal intensity was on average 1.8-points higher in O_2-MAP foods than in N_2-MAP foods, which also had effects on the atomic environment of the iron. The analysis of correlations between iron, P and S suggests that ferritin, phytates, and sulfur-containing amino acids may be involved in iron binding and consequently affect its bioavailability. XANES spectroscopy highlighted spectral signatures specific to the animal and plant mixtures used, with an energy position centroid of 7114.14 eV for plant-source mixtures and 7113.82 eV for animal-source mixtures, and an integrated pre-edge intensity of 0.48 for plant-source mixtures and 0.15 for animal-source mixtures. μ-XANES spectroscopy revealed interactions between animal and plant parts during food storage, either through iron diffusion and/or changes in iron speciation.

The iron-rich hybrid 3D-printed food studied here is suitable for people suffering from iron deficiency because of the amount of iron it provides, but it remains sensitive to storage conditions, which will need to be adapted in terms of atmosphere and shelf life. Further investigations, in particular *in vivo* experiments, would be valuable to assess iron bioavailability on a whole-food scale.

This work used synchrotron X-rays to more thoroughly characterize dietary iron and its atomic environment in a new type of complex food, something that had never been done before. This research thus opens new perspectives for the use of this type of analysis as a step towards engineering tomorrow's food.

CRediT authorship contribution statement

Coline Schiell: Writing – original draft, Methodology, Investigation, Funding acquisition, Formal analysis, Conceptualization. **Camille Rivard:** Writing – review & editing, Software, Resources, Methodology, Investigation, Formal analysis. **Stéphane Portanguen:** Writing – review & editing, Investigation, Conceptualization. **Valérie Scislowski:** Writing – review & editing, Funding acquisition, Conceptualization. **Pierre-Sylvain Mirade:** Writing – review & editing, Supervision, Project administration, Funding acquisition, Conceptualization. **Thierry Astruc:** Writing – review & editing, Supervision, Project administration, Funding acquisition, Conceptualization.

Declaration of competing interest

The authors declare the following financial interests/personal relationships which may be considered as potential competing interests: Schiell reports financial support was provided by BPI (Public bank for investment France). Schiell reports financial support was provided by National Association of Technical Research. Portanguen reports equipment, drugs, or supplies was provided by SOLEIL. If there are other authors, they declare that they have no known competing financial

interests or personal relationships that could have appeared to influence the work reported in this paper.

Data availability

Data will be made available on request.

Acknowledgments

Appendix A. Supplementary data

Supplementary data to this article can be found online at https://doi.org/10.1016/j.foodchem.2024.141058.

References

Ahn, D. U., Wolfe, F. H., & Sim, J. S. (1993). Three methods for determining nonheme iron in Turkey meat. *Journal of Food Science, 58*(2), 288–291. https://doi.org/10.1111/j.1365-2621.1993.tb04257.x

Archundia-Herrera, M. C., Nunes, I. D., Barrios, I. D., Park, C. Y., Bell, R. C., & O'Brien, K. O. (2024). Development of a database for the estimation of heme iron and nonheme iron content of animal-based foods. *Current Developments in Nutrition, 8*(4), Article 102130. https://doi.org/10.1016/j.cdnut.2024.102130

Bohn, L., Meyer, A. S., & Rasmussen, Søren. K. (2008). Phytate : Impact on environment and human nutrition. A challenge for molecular breeding. *Journal of Zhejiang University SCIENCE B, 9*(3), 165–191. https://doi.org/10.1631/jzus.B0710640.

Briat, J.-F., Duc, C., Ravet, K., & Gaymard, F. (2010). Ferritins and iron storage in plants. *Biochimica et Biophysica Acta (BBA), 1800*(8), 806–814. https://doi.org/10.1016/j.bbagen.2009.12.003

Chang, X., Lv, C., & Zhao, G. (2023). A dual function of ferritin (animal and plant): Its holo form for iron supplementation and apo form for delivery systems. *Annual Review of Food Science and Technology, 14*(1), 113–133. https://doi.org/10.1146/annurev-food-060721-024902

Cherian, G., Fraz, A., & Bionaz, M. (2023). Evaluating the impact of organic chromium on hepatic phospholipid fatty acid molecular species, transcription of genes associated with lipid metabolism and oxidative status in broiler chickens fed flaxseed. *Poultry Science, 102*(10), Article 102976. https://doi.org/10.1016/j.psj.2023.102976

Collman, J. P., Gagne, R. R., Reed, C. A., Robinson, W. T., & Rodley, G. A. (1974). Structure of an iron(II) dioxygen complex; a model for oxygen carrying hemoproteins. *Proceedings of the National Academy of Sciences, 71*(4), 1326–1329. https://doi.org/10.1073/pnas.71.4.1326

Consalez, F., Ahern, M., Andersen, P., & Kjellevold, M. (2022). The effect of the meat factor in animal-source foods on micronutrient absorption: A scoping review. *Advances in Nutrition, 13*(6), 2305–2315. https://doi.org/10.1093/advances/nmac089

De Brier, N., Gomand, S. V., Donner, E., Paterson, D., Smolders, E., Delcour, J. A., & Lombi, E. (2016). Element distribution and iron speciation in mature wheat grains (*Triticum aestivum* L.) using synchrotron X-ray fluorescence microscopy mapping and X-ray absorption near-edge structure (XANES) imaging. *Plant, Cell & Environment, 39*(8), 1835–1847. https://doi.org/10.1111/pce.12749

Estévez, M., Geraert, P.-A., Liu, R., Delgado, J., Mercier, Y., & Zhang, W. (2020). Sulphur amino acids, muscle redox status and meat quality: More than building blocks – Invited review. *Meat Science, 163*, Article 108087. https://doi.org/10.1016/j.meatsci.2020.108087

Grillet, L., Ouerdane, L., Flis, P., Hoang, M. T. T., Isaure, M.-P., Lobinski, R., … Mari, S. (2014). Ascorbate efflux as a new strategy for iron reduction and transport in plants. *Journal of Biological Chemistry, 289*(5), 2515–2525. https://doi.org/10.1074/jbc.M113.514828

Hasegawa, N., Takahashi, Y., & Itai, T. (2023). Tissue-variation of iron stable isotopes in marine fish coupled with speciation analysis using X-ray absorption fine structure. *Science of the Total Environment, 881*, Article 163449. https://doi.org/10.1016/j.scitotenv.2023.163449

Henderson, G. S., de Groot, F. M. F., & Moulton, B. J. A. (2014). X-ray absorption near-edge structure (XANES) spectroscopy. *Reviews in Mineralogy and Geochemistry, 78*(1), 75–138. https://doi.org/10.2138/rmg.2014.78.3

Hoppler, M., Zeder, C., & Walczyk, T. (2009). Quantification of ferritin-bound iron in plant samples by isotope tagging and species-specific isotope dilution mass spectrometry. *Analytical Chemistry, 81*(17), 7368–7372. https://doi.org/10.1021/ac900885j

Hornsey, H. C. (1956). The colour of cooked cured pork. I.—Estimation of the nitric oxide-haem pigments. *Journal of the Science of Food and Agriculture, 7*(8), 534–540. https://doi.org/10.1002/jsfa.2740070804

Institute of Medicine. (2001). *Dietary Reference Intakes for Vitamin A, Vitamin K, Arsenic, Boron, Chromium, Copper, Iodine, Iron, Manganese, Molybdenum, Nickel, Silicon, Vanadium, and Zinc*. Washington, DC: The National Academies Press. https://doi.org/10.17226/10026

Landrot, G. (2018). *FASTOSH: a software to process XAFS data for geochemical & environmental applications*. In Goldschmidt (Ed.) (p. 1402). Boston.

Leonhardt, M., & Wenk, C. (1997). Variability of selected vitamins and trace elements of different meat cuts. *Journal of Food Composition and Analysis, 10*(3), 218–224. https://doi.org/10.1006/jfca.1997.0536

Li, C., Qi, X., Li, M., Zhao, G., & Hu, X. (2009). Phosphate facilitates Fe(II) oxidative deposition in pea seed (Pisum sativum) ferritin. *Biochimie, 91*(11–12), 1475–1481. https://doi.org/10.1016/j.biochi.2009.08.007

Lv, C., Zhao, G., & Lönnerdal, B. (2015). Bioavailability of iron from plant and animal ferritins. *The Journal of Nutritional Biochemistry, 26*(5), 532–540. https://doi.org/10.1016/j.jnutbio.2014.12.006

Makowska, A., Zielińska-Dawidziak, M., Niedzielski, P., & Michalak, M. (2018). Effect of extrusion conditions on iron stability and physical and textural properties of corn snacks enriched with soybean ferritin. *International Journal of Food Science & Technology, 53*(2), 296–303. https://doi.org/10.1111/ijfs.13585

Mazumder, K., Biswas, B., Kerr, P. G., Blanchard, C., Nabila, A., Golder, M., … Farahnaky, A. (2021). Comparative assessment of nutritional, thermal, rheological and functional properties of nine Australian lupin cultivars. *Scientific Reports, 11*(1), 21515. https://doi.org/10.1038/s41598-021-00838-x.

Mullen, A. M., & Álvarez, C. (2016). Offal: Types and composition. In *Encyclopedia of food and health* (pp. 152–157). Elsevier. https://doi.org/10.1016/B978-0-12-384947-2.00501-8.

O'Flaherty, E. A. A., Tsermoula, P., O'Neill, E. E., & O'Brien, N. M. (2019). Co-products of beef processing enhance non-haem iron absorption in an *in vitro* digestion/caco-2 cell model. *International Journal of Food Science & Technology, 54*(4), 1256–1264. https://doi.org/10.1111/ijfs.14049

Piskin, E., Cianciosi, D., Gulec, S., Tomas, M., & Capanoglu, E. (2022). Iron absorption: Factors, limitations, and improvement methods. *ACS Omega, 7*(24), 20441–20456. https://doi.org/10.1021/acsomega.2c01833

Podder, R., Glahn, R. P., & Vandenberg, A. (2021). Dual-fortified lentil products—A sustainable new approach to provide additional bioavailable iron and zinc in humans. *Current developments. Nutrition, 5*(2), nzab004. https://doi.org/10.1093/cdn/nzab004

Pongrac, P., Scheers, N., Sandberg, A.-S., Potisek, M., Arčon, I., Kreft, I., Kump, P., & Vogel-Mikuš, K. (2016). The effects of hydrothermal processing and germination on Fe speciation and Fe bioaccessibility to human intestinal Caco-2 cells in Tartary buckwheat. *Food Chemistry, 199*, 782–790. https://doi.org/10.1016/j.foodchem.2015.12.071

Quinteros, A., Farré, R., & Lagarda, M. J. (2001). Optimization of iron speciation (soluble, ferrous and ferric) in beans, chickpeas and lentils. *Food Chemistry, 75*(3), 365–370. https://doi.org/10.1016/S0308-8146(01)00214-X

Schiell, C., Portanguen, S., Scislowski, V., Astruc, T., & Mirade, P.-S. (2023). Investigation into the physicochemical and textural properties of an iron-rich 3D-printed hybrid food. *Foods, 12*(7), 1375.

Schindelin, J., Arganda-Carreras, I., Frise, E., Kaynig, V., Longair, M., Pietzsch, T., … Cardona, A. (2012). Fiji: An open-source platform for biological-image analysis. *Nature Methods, 9*(7), 676–682. https://doi.org/10.1038/nmeth.2019

Seong, P. N., Cho, S. H., Park, K. M., Kang, G. H., Park, B. Y., Moon, S. S., & Ba, H. V. (2015). Characterization of Chicken By-products by Mean of Proximate and Nutritional Compositions. *Korean Journal for Food Science of Animal Resources, 35*(2), 179–188. https://doi.org/10.5851/kosfa.2015.35.2.179

Shubham, K., Anukiruthika, T., Dutta, S., Kashyap, A. V., Moses, J. A., & Anandharamakrishnan, C. (2020). Iron deficiency anemia: A comprehensive review on iron absorption, bioavailability and emerging food fortification approaches. *Trends in Food Science & Technology, 99*, 58–75. https://doi.org/10.1016/j.tifs.2020.02.021

Singh, P., & Prasad, S. (2018). Determination of ascorbic acid and its influence on the bioavailability of iron, zinc and calcium in Fijian food samples. *Microchemical Journal, 139*, 119–124. https://doi.org/10.1016/j.microc.2018.02.019

Singh, S. P., Vogel-Mikuš, K., Arčon, I., Vavpetič, P., Jeromel, L., Pelicon, P., … Tuli, R. (2013). Pattern of iron distribution in maternal and filial tissues in wheat grains with contrasting levels of iron. *Journal of Experimental Botany, 64*(11), 3249–3260. https://doi.org/10.1093/jxb/ert160

Solé, V. A., Papillon, E., Cotte, M., Walter, P., & Susini, J. (2007). A multiplatform code for the analysis of energy-dispersive X-ray fluorescence spectra. *Spectrochimica Acta Part B: Atomic Spectroscopy, 62*(1), 63–68. https://doi.org/10.1016/j.sab.2006.12.002

Srivastava, A. K., Reutovich, A. A., Hunter, N. J., Arosio, P., & Bou-Abdallah, F. (2023). Ferritin microheterogeneity, subunit composition, functional, and physiological implications. *Scientific Reports, 13*(1), 19862. https://doi.org/10.1038/s41598-023-46880-9

Tomovic, V., Jokanovic, M., Sojic, B., Skaljac, S., Tasic, T., & Ikonic, P. (2015). Minerals in pork meat and edible offal. *Procedia Food Science, 5*, 293–295. https://doi.org/10.1016/j.profoo.2015.09.083

Vantelon, D., Trcera, N., Roy, D., Moreno, T., Mailly, D., Guilet, S., Metchalkov, E., Delmotte, F., Lassalle, B., Lagarde, P., & Flank, A.-M. (2016). The LUCIA beamline at SOLEIL. *Journal of Synchrotron Radiation, 23*(2), 635–640. https://doi.org/10.1107/S1600577516000746

WHO. (2019). *Anaemia in women and children. The Global Health Observatory*. Retrieved from https://www.who.int/data/gho/data/indicators/ Accessed April 8, 2024.

Wilke, M., Farges, F., Petit, P.-E., Brown, G. E., & Martin, F. (2001). Oxidation state and coordination of Fe in minerals: An Fe *K*-XANES spectroscopic study. *American Mineralogist, 86*(5–6), 714–730. https://doi.org/10.2138/am-2001-5-612

Wilson, S. A., Green, E., Mathews, I. I., Benfatto, M., Hodgson, K. O., Hedman, B., & Sarangi, R. (2013). X-ray absorption spectroscopic investigation of the electronic structure differences in solution and crystalline oxyhemoglobin. *Proceedings of the National Academy of Sciences, 110*(41), 16333–16338. https://doi.org/10.1073/pnas.1315734110

Wojdyr, M. (2010). Fityk: A general-purpose peak fitting program. *Journal of Applied Crystallography, 43*(5), 1126–1128. https://doi.org/10.1107/S002188981003049

Yildiz, E. (2023). Characterization of fruit vinegars via bioactive and organic acid profile using Chemometrics. *Foods, 12*(20), 3769. https://doi.org/10.3390/foods12203769

Yruela, I. (2013). *Transition metals in plant photosynthesis. Metallomics, 5*(9), 1090. https://doi.org/10.1039/c3mt00086a

Zhao, G. (2010). Phytoferritin and its implications for human health and nutrition. *Biochimica et Biophysica Acta, 1800*(8), 815–823. https://doi.org/10.1016/j.bbagen.2010.01.009

Zielińska-Dawidziak, M., Białas, W., Piasecka-Kwiatkowska, D., Staniek, H., & Niedzielski, P. (2023). Digestibility of protein and iron availability from enriched legume sprouts. *Plant Foods for Human Nutrition, 78*(2), 270–278. https://doi.org/10.1007/s11130-023-01045-x